



Analysis of nonisothermal screw extrusion processing of viscoplastic fluids with significant back flow

Adeniyi Lawal^{a,*}, Dilhan M. Kalyon^b

^a Department of Chemical Engineering, King Fahd University of Petroleum and Minerals, Dhahran 31261, Saudi Arabia

^b Department of Chemical, Biochemical, and Materials Engineering, Highly Filled Materials Institute, Stevens Institute of Technology, Castle Point, Hoboken, NJ 07030, USA

Received 30 May 1997; accepted 29 October 1998

Abstract

Analytical solutions are developed for the flow and heat transfer in nonisothermal screw extrusion processing of viscoplastic fluids with pressure back flow. The screw geometry is assumed to be shallow and the flight width small, thus enabling the flow to be modeled as that occurring between two infinitely long parallel plates, i.e., the generalized Couette flow. The constitutive equation is the generalized Newtonian fluid and the Herschel–Bulkley viscosity function is used to describe the rheology of the viscoplastic fluid, and the interfacial boundary condition of wall slip is incorporated in the analysis. For the temperature problem, the shear viscosity of the fluid is taken to be independent of temperature, and the equation of conservation of energy is reduced to an eigenvalue problem. The eigenfunctions and eigenvalues are determined using the Runge–Kutta method. The analytical solutions in terms of pressure gradient, and temperature distributions show good agreement with numerical and experimental results in the literature for power law fluids. The analytical results are also compared with experimental data collected from twin screw extrusion processing of a concentrated suspension which exhibits viscoplasticity, and wall slip, with the mass flow rate sufficiently low for the pressure back flow to be significant. © 1999 Published by Elsevier Science Ltd. All rights reserved.

Keywords: Nonisothermal extrusion; Viscoplastic; Slip backflow

1. Introduction

The single-screw and twin-screw extruders are used for a variety of continuous processing tasks such as melting, pressurization, mixing, blending, compounding, and reactive extrusion. They rely on drag-induced flow, and pressurization whereby the fluid is conveyed and pressurized by the action of a moving surface. The highly viscous nature of processed materials generally encountered including concentrated suspensions and polymeric composites implies significant viscous dissipation in extruders. The isothermal extrusion flow of polymeric fluids has been studied by a number of investigators (Denson and Hwang, 1980; Wang and White, 1989; Kalyon et al., 1988; Lai-Fook et al., 1989; Lawal and Kalyon, 1994a) using different mathematical models, and Fenner (1969) investigated the various solution methods

available for the flow and deformation occurring in the single-screw extruder and compared the findings with experimental results. The geometry of the extruder is usually unwound in the channel direction, and the curvature effects neglected. Zamodits and Pearson (1969) presented screw characteristic curves for a rectangular channel for different values of the power-law index. Denson and Hwang (1980), using the finite element method (FEM), analyzed the flow in the twin-screw extruder for several actual channel geometries, but the fluid was assumed to be Newtonian. For shallow-screw geometries, the curvature effects in single-screw and twin-screw extruders can be neglected without incurring significant errors, and for such screw geometries, the flow so obtained, i.e., the generalized plane Couette flow appears to provide an excellent model description of the flow. Closed-form analytical expressions can then be easily worked out for the velocity distribution, and hence the functional dependence of the throughput rate on the pressure generated, for various design parameters and operating conditions. For constant property fluids, the

* Corresponding author. Tel.: 00966 03 860 2205; fax: 00966 03 860 4234.

E-mail address: awlawal@dpc.kfupm.edu.sa (A.Lawal).

thermal problem can also be similarly handled. In the nonisothermal analysis of screw extrusion, viscous dissipation and heat conduction in the direction of screw depth were the first effects to be considered (Colwell and Nicholls, 1959). Subsequently, heat conduction in the transverse direction (Griffith, 1962) and, more recently, heat convection in the downchannel direction (Kwon et al., 1991) were included in the solution of the equation of energy.

Among the many applications of screw extruders, the processing of filled polymers and concentrated suspensions deserves special attention. The processing and simulation of the continuous processing of such filled systems are affected by the observed viscoplasticity (Bird et al., 1983) and the wall slip behavior of such systems (Yilmazer and Kalyon, 1989; Kalyon et al., 1993; Aral and Kalyon, 1994). Special rheological methods are required for the characterization of the viscoplasticity and wall slip behavior of concentrated suspensions (Yilmazer and Kalyon, 1989; Kalyon et al., 1993, Aral and Kalyon, 1994, 1995). Previous studies have demonstrated that wall slip plays a very prominent role in determining the extrudability of concentrated suspensions. Thus, a realistic model for the processing of these viscoplastic materials should incorporate the wall slip boundary condition at solid surfaces.

Here, we present analytical and exact solutions for the velocity and temperature distributions which are applicable to nonisothermal single and twin-screw extrusion processing of viscoplastic fluids with wall slip. Various simplifications of the Herschel–Bulkley viscoplastic fluid viscosity function, i.e., the Bingham plastic, the power-law fluid of Ostwald–de Waele, and the Newtonian fluid, can be accommodated. The pressurization and heat transfer occurring in the single-screw extruder, and in the regular flighted screw sections of the co-rotating twin-screw extruder during the processing of concentrated suspensions will be focused upon with the flow and heat transfer modeled as that occurring between two infinite parallel plates representing the screw and barrel surfaces. The problem of solving the equation of conservation of energy is transformed to that of solving an eigenvalue problem. As many eigenvalues and eigenfunctions as required are determined using the Runge–Kutta method. We also compare the analytical results with experimental extrusion processing data on concentrated suspensions collected from an industrial scale extruder at low mass flow rate with significant pressure back flow.

2. Analysis

Fig. 1a shows a typical self-wiping co-rotating fully intermeshing and regular (full) flighted screw configuration. For self-wiping elements with small flight width, the

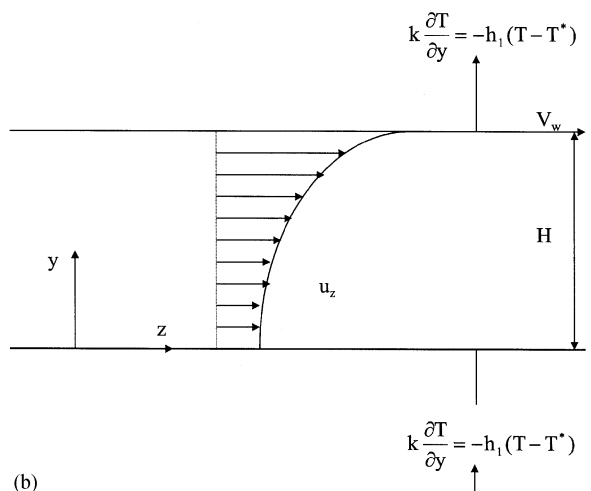
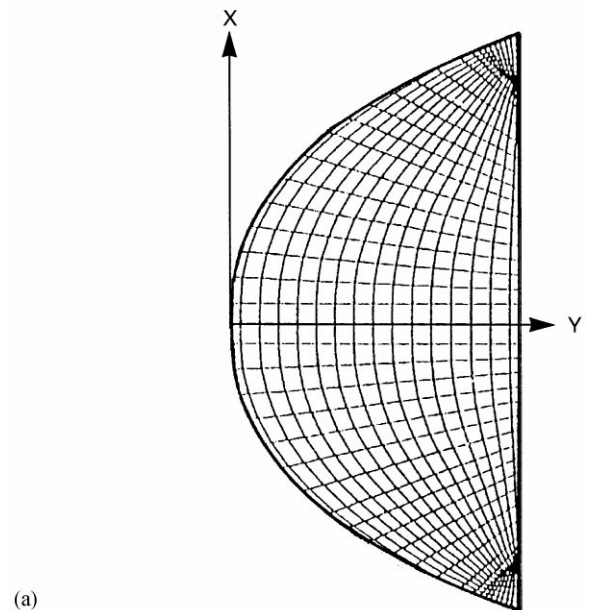
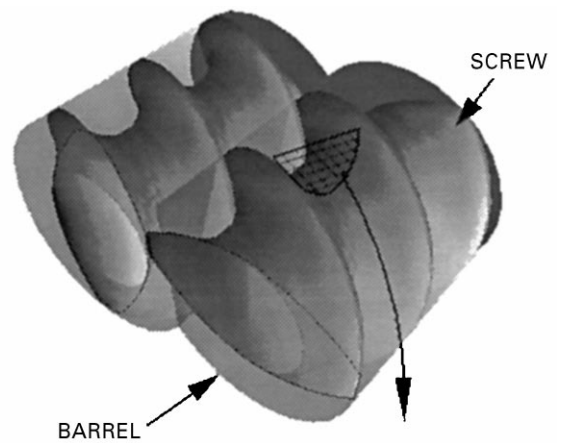


Fig. 1. (a) Geometry of a co-rotating twin-screw extruder. (b) Schematic of the considered model of extrusion flow with the fluid entering at $z = 0$ with specified inlet temperature $c(y)$ and fully developed velocity $u_z(y)$.

two screw elements can be assumed to form continuous-flow channels from one screw to the other. If the effect of curvature is neglected, and the channel and barrel are unwound in the helical direction of the screw, the steady non-isothermal flow of a viscoplastic fluid in the twin-screw extruder can be modeled as that occurring in a channel formed by two parallel plates in relative motion, thus enabling the use of Cartesian coordinate system. The coordinate axis is placed on the screw and the screw is treated as stationary while the barrel moves relative to the screw at an angle (i.e. the helix angle) with respect to the downchannel direction. With all the foregoing assumptions, the co-rotating twin-screw extruder with self-wiping elements and small flight width essentially becomes a row of adjacent parallel channels, similar to what obtains in the modeling of single-screw extruder, and the total throughput is taken as the sum of the individual throughput from each channel. For the two-tipped screw elements in a twin-screw extruder, the number of such parallel channels is three (Booy, 1978). The inertia effect is usually negligible because of the highly viscous nature of the viscoplastic materials used in extrusion and the low Reynolds number of the resulting flow. In addition, viscoplastic liquids generally have low thermal conductivity and moderately high value of heat capacity, and hence exhibit high Prandtl numbers. In essence, the flow field will require a very short distance to attain a fully developed condition in comparison with the temperature field. Therefore, the flow can be accurately modeled as hydrodynamically developed but thermally developing at the entrance to the extruder. Related to this is the high Péclet number ($Pe > 10^3$) associated with polymer processing operations which enables the neglect of heat conduction in the downchannel direction except for very low-volume flow rates and the region very close to the entrance.

The fluid enters the screw channel of depth H (Fig. 1b) with a known temperature distribution and flows in the downchannel direction with the viscous heat generating local temperature variations in both y and z directions. On both the screw surface and the barrel, the heat flux will be given by a heat transfer coefficient thus permitting various thermal boundary conditions, including as limiting cases, the isothermal and the adiabatic conditions. Variations of the physical properties of the fluid (such as the shear viscosity, density and heat capacity) due to temperature are assumed negligible, hence the thermal and momentum problems are decoupled.

2.1. Velocity field

The equation of conservation of momentum for this one-dimensional flow is given by

$$-\frac{d\tau_{yz}}{dy} = \frac{dP}{dz}, \tag{1}$$

where y is the transverse coordinate, P is the pressure, τ_{yz} is the shearing stress and compressive stresses are positive. In the screw extruder, dP/dz is positive for dynamic viscous pressurization. In Eq. (1), the rheology of the fluid is assumed to be described by the Herschel–Bulkley viscosity function

$$\tau_{yz} = -m \left| \frac{du_z}{dy} \right|^{n-1} \frac{du_z}{dy} \pm \tau_o, \quad |\tau_{yz}| \geq \tau_o, \tag{2a}$$

$$\frac{du_z}{dy} = 0, \quad |\tau_{yz}| \leq \tau_o, \tag{2b}$$

where m and n are material parameters and τ_o is the yield stress.

Defining the following dimensionless variables:

$$u_z^* = \frac{u_z}{V_w}, \quad \xi = \frac{y}{H}, \quad A = \left(\frac{H^{n+1}}{mV_w^n} \right) \frac{dP}{dz}. \tag{3a}$$

Eq. (1) becomes

$$\frac{d}{d\xi} \left(\left| \frac{du_z^*}{d\xi} \right|^{n-1} \frac{du_z^*}{d\xi} \right) = A. \tag{3b}$$

Eq. 3(b) is applicable only in the deformation region and is replaced by the rigid-body translation requirement, Eq. 2(b), in the plug region whenever it exists. The boundary conditions to Eq. 3(b) are provided by the Navier’s slip at the wall condition which is of the form (Silliman and Scriven, 1980):

$$\mathbf{t} \cdot (\mathbf{u} - \mathbf{u}_{\text{solid}}) = \beta \mathbf{n} \cdot \boldsymbol{\pi} \tag{4}$$

where \mathbf{t} is the unit tangent vector to the surface, \mathbf{n} the unit outward normal, and β is the slip parameter. The limits for $\beta = \infty$ and $\beta = 0$ give perfect slip and no slip conditions, respectively. \mathbf{u} and $\mathbf{u}_{\text{solid}}$ are the velocity vectors of the fluid and the solid surface respectively, and $\boldsymbol{\pi}$ is the total stress tensor.

Returning to Eq. 3(b), three distinct cases are possible (Fig. 2), depending on the values of the parameters of the problem. The solutions to these cases have been worked out by Lawal and Kalyon (1994a) and are as follows:

Case A: No plug region. This case is obtained when

$$\frac{A^s}{(s+1)} \leq 1 - \kappa_1 - \kappa_2 + \alpha_2 \tag{5a}$$

and the velocity distribution is

$$u_z^* = \frac{A^s}{(s+1)} (\xi - \lambda_2)^{s+1} - \frac{A^s}{(s+1)} (-\lambda_2)^{s+1} + \kappa_1 + \alpha_1 \lambda_2, \tag{5b}$$

$$0 \leq \xi \leq 1.$$

The parameter λ_2 is obtained from

$$\frac{A^s}{(s+1)} (1 - \lambda_2)^{s+1} - \frac{A^s}{(s+1)} (-\lambda_2)^{s+1} + \kappa_1 + \alpha_1 \lambda_2 + \kappa_2 + \alpha_2 (\lambda_2 - 1) - 1 = 0. \tag{5c}$$

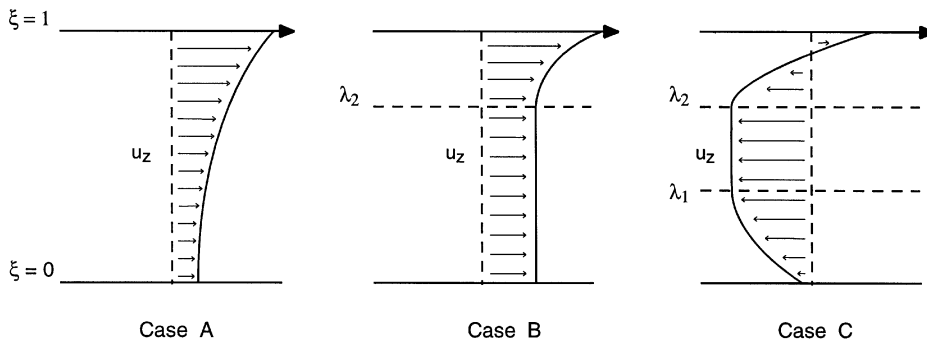


Fig. 2. Schematic representation of the velocity profiles for the three cases for positive pressure gradient.

In these equations and all the ones to be presented subsequently, we have $s = 1/n$, $\kappa_1 = \beta_b \tau_o / V_w$, $\alpha_1 = (\beta_b H / V_w) (-dP/dz)$, $\kappa_2 = \beta_t \tau_o / V_w$, and $\alpha_2 = (\beta_t H / V_w) (-dP/dz)$. β_b and β_t are the slip parameters at the bottom and top surfaces, respectively.

Case B: Plug attached to the bottom surface.

$$u_z^* = 1 - \frac{A^s}{(s+1)} (1 - \lambda_2)^{s+1} - \kappa_2 - \alpha_2 (\lambda_2 - 1),$$

$$0 \leq \xi \leq \lambda_2, \tag{6a}$$

$$u_z^* = \frac{A^s}{(s+1)} (\xi - \lambda_2)^{s+1} - \frac{A^s}{(s+1)} (1 - \lambda_2)^{s+1} - \kappa_2 - \alpha_2 (\lambda_2 - 1) + 1, \quad \lambda_2 \leq \xi \leq 1 \tag{6b}$$

λ_2 is given by the equation

$$\frac{A^s}{(s+1)} (1 - \lambda_2)^{s+1} + \kappa_1 + \alpha_1 \lambda_2 + \kappa_2 + \alpha_2 (\lambda_2 - 1) - 1 = 0. \tag{6c}$$

The following processing conditions must be met for Case B to occur:

$$\frac{A^s}{(s+1)} \geq 1 - \kappa_1 - \kappa_2 + \alpha_2, \tag{7a}$$

$$\lambda_2 - \lambda_1 = \left(\frac{2\tau_o}{HdP/dz} \right) \geq 1 \tag{7b}$$

or

$$\lambda_2 - \lambda_1 \geq \lambda^*, \tag{7c}$$

where λ^* is determined from:

$$\frac{A^s}{(s+1)} (1 - \lambda^*)^{s+1} + \kappa_1 + \alpha_1 \lambda^* + \kappa_2 + \alpha_2 (\lambda^* - 1) - 1 = 0. \tag{7d}$$

Case C: Floating plug region

$$u_z^* = \frac{A^s}{(s+1)} (\lambda_1 - \xi)^{s+1} - \frac{A^s}{(s+1)} \lambda_1^{s+1} + \kappa_1 + \alpha_1 \lambda_2,$$

$$0 \leq \xi \leq \lambda_1, \tag{8a}$$

$$u_z^* = 1 - \frac{A^s}{(s+1)} (1 - \lambda_2)^{s+1} - \kappa_2 + \alpha_2 (\lambda_2 - 1),$$

$$\lambda_1 \leq \xi \leq \lambda_2, \tag{8b}$$

$$u_z^* = \frac{A^s}{(s+1)} (\xi - \lambda_2)^{s+1} - \frac{A^s}{(s+1)} (1 - \lambda_2)^{s+1} - \kappa_2 - \alpha_2 (\lambda_2 - 1) + 1, \quad \lambda_2 \leq \xi \leq 1. \tag{8c}$$

The equation for λ_2 is provided by

$$1 - \frac{A^s}{(s+1)} (1 - \lambda_2)^{s+1} - \kappa_1 - \alpha_1 \lambda_2 - \kappa_2 - \alpha_2 (\lambda_2 - 1) + \frac{A^s}{(s+1)} \left(\lambda_2 - \frac{2\tau_o}{HdP/dz} \right)^{s+1} = 0, \tag{8d}$$

and λ_1 subsequently obtained from

$$\lambda_2 - \lambda_1 = \frac{2\tau_o}{HdP/dz}. \tag{8e}$$

The processing conditions that will give rise to Case C are given by Eq. 7(a) and

$$\lambda_2 - \lambda_1 \leq \lambda^* \tag{9}$$

with λ^* again determined from Eq. 7(d).

2.2. Temperature field

With the assumptions given earlier, the thermal problem is described by the equation

$$\rho C_p u_z \frac{\partial T}{\partial z} = k \frac{\partial^2 T}{\partial y^2} + \eta |\dot{\gamma}|^2 \tag{10a}$$

subject to the following conditions:

$$T = c(y), \quad z = 0, 0 \leq y \leq H, \tag{10b}$$

$$k \frac{\partial T}{\partial y} = h_0(T - T^*), \quad z > 0, y = 0, \tag{10c}$$

$$k \frac{\partial T}{\partial y} = -h_1(T - T^*), \quad z > 0, y = H. \tag{10d}$$

In Eqs. (10), η is the shear viscosity which is obtainable from Eq. (2a), $|\dot{\gamma}|$ is the magnitude of the rate-of-deformation tensor, $c(y)$ is the inlet temperature distribution, and T^* is a reference temperature. To render the equations dimensionless, we define the following variables:

$$\theta = \frac{T - T^*}{\Delta T}, \tag{11a}$$

$$z^* = z/H \text{ Péc}, \tag{11b}$$

$$\tau_o^* = \tau_o/m(V_w/H)^n, \tag{11c}$$

where $\text{Péc} = \rho C_p V_w H/k$ is the Péclet number and ΔT is a reference temperature difference. On substituting for η and $|\dot{\gamma}|$ in terms of the velocity gradient, and introducing the dimensionless variables, Eqs. (10) become

$$u_z^* \frac{\partial \theta}{\partial z^*} = \frac{\partial^2 \theta}{\partial \xi^2} + Gf(\xi), \tag{12a}$$

$$\theta = C(\xi), \quad z^* = 0, 0 \leq \xi \leq 1, \tag{12b}$$

$$\frac{\partial \theta}{\partial \xi} = +Bi_0 \theta, \quad z^* > 0, \xi = 0, \tag{12c}$$

$$\frac{\partial \theta}{\partial \xi} = -Bi_1 \theta, \quad z^* > 0, \xi = 1, \tag{12d}$$

where $G = m (V_w/H)^{n-1} V_w^2/k\Delta T$ is the Griffith number (generally referred to as the Brinkmann number for the Newtonian fluid), $Bi_0 = h_0 H/k$, $Bi_1 = h_1 H/k$ are Biot moduli and $f(\xi)$, the viscous dissipation function is given by

$$f(\xi) = \left| \frac{du_z^*}{d\xi} \right|^{n+1} + \tau_o^* \left| \frac{du_z^*}{d\xi} \right|. \tag{13}$$

The velocity gradient can be evaluated from the appropriate equation of any of those earlier presented.

In the analysis that follows, we need to treat the adiabatic problem where both Bi_0 and Bi_1 are zero differently from all other possible cases where at least one of the heat transfer coefficients has a non-zero value. For the latter conditions, at a sufficiently large downchannel distance, a temperature distribution will be attained which depends only on the transverse coordinate ξ . However, for the adiabatic condition, the temperature distribution will continue to grow without bounds as we proceed downchannel, since there is no mechanism at the wall surfaces that allows for the removal of the viscous energy generated.

2.3. Non-zero biot moduli

When at least one of the Biot moduli is non-zero, we can assume a solution of the form

$$\theta(\xi, z^*) = \theta_1(\xi) - \sum_m a_m \psi_m(\xi) \exp(-\lambda_m z^*), \tag{14}$$

where θ_1 is the temperature profile far downstream and is obtainable from the solution to the following ordinary differential equation

$$\frac{d^2 \theta_1}{d\xi^2} = -Gf(\xi) \tag{15a}$$

subject to the following boundary conditions:

$$\left. \frac{d\theta_1(\xi)}{d\xi} \right|_{\xi=0} = Bi_0 \theta_1(0), \tag{15b}$$

$$\left. \frac{d\theta_1(\xi)}{d\xi} \right|_{\xi=1} = -Bi_1 \theta_1(1). \tag{15c}$$

The solution to Eq. (15) in its general form is

$$\theta_1(\xi) = \int_0^\xi (\xi' - \xi) Gf(\xi') d\xi' - (b_1 \xi + b_3) \int_0^1 (\xi' - 1) Gf(\xi') d\xi' + (b_2 \xi + b_4) \int_0^1 Gf(\xi') d\xi', \tag{16}$$

where the coefficients b_1 – b_4 are given in Table 1 for all possible combinations of values that can be assumed by the Biot moduli. In Table 1, finite values include zero

Table 1
Coefficients b_1 – b_4 for the temperature solution θ_1

Bi_0	Bi_1	b_1	b_2	b_3	b_4
Finite	Finite	$\frac{Bi_0 Bi_1}{Bi_0 + Bi_1 + Bi_0 Bi_1}$	$\frac{Bi_0}{Bi_0 + Bi_1 + Bi_0 Bi_1}$	$\frac{Bi_1}{Bi_0 + Bi_1 + Bi_0 Bi_1}$	$\frac{1}{Bi_0 + Bi_1 + Bi_0 Bi_1}$
∞	Finite	$Bi_1/(1 + Bi_1)$	$1/(1 + Bi_1)$	0	0
Finite	∞	$Bi_0/(1 + Bi_0)$	0	$1/(1 + Bi_0)$	0
∞	∞	1	0	0	0

with the exception of the adiabatic case which will be handled below separately.

To obtain the developing part of the temperature profile, we substitute the assumed temperature solution (Eq. (14)) into the energy equation (Eq. (12a)), and obtain the following eigenvalue problem:

$$\frac{d^2\psi_m(\xi)}{d\xi^2} + \lambda_m u_z^* \psi_m(\xi) = 0 \quad (17a)$$

subject to the conditions

$$\left. \frac{d\psi_m(\lambda_m, \xi)}{d\xi} \right|_{\xi=0} = Bi_0 \psi_m(0) \quad (17b)$$

$$\left. \frac{d\psi_m(\lambda_m, \xi)}{d\xi} \right|_{\xi=1} = -Bi_1 \psi_m(1) \quad (17c)$$

with ψ_m and λ_m being the eigenfunctions and eigenvalues, respectively. The eigenvalue problem (Eq. (17)) can be solved for ψ_m and λ_m , and subsequently the expansion coefficients a_m can be determined from the entrance condition (Eq. (12b)):

$$\sum_m a_m \psi_m(\xi) = \theta_1(\xi) - C(\xi). \quad (18)$$

Eq. (18) is first multiplied by $u_z^* \psi_n$ and then integrated over the transverse coordinate ξ from 0 to 1 to obtain

$$a_n \int_0^1 u_z^* \psi_n^2(\xi) d\xi = \int_0^1 (\theta_1(\xi) - C(\xi)) u_z^* \psi_n(\xi) d\xi - \sum_{\substack{m=1 \\ m \neq n}}^1 a_m \int_0^1 u_z^* \psi_m(\xi) \psi_n d\xi. \quad (19)$$

The second term on the right-hand side of Eq. (19) can be shown to be equal to zero by multiplying Eq. (17a) by ψ_n and integrating over ξ from 0 to 1. The expansion coefficients a_m will therefore be given by

$$a_m = \frac{\int_0^1 (\theta_1(\xi) - C(\xi)) u_z^* \psi_m(\xi) d\xi}{\int_0^1 u_z^* \psi_m^2(\xi) d\xi}. \quad (20)$$

2.4. Adiabatic wall surfaces

When both Bi_0 and Bi_1 are zero, we expect a temperature profile that will never be invariant with downchannel distance, therefore we postulate a solution of the form

$$\theta(\xi, z^*) = \theta_1(\xi) + Dz^* - \sum_m a_m \psi_m(\xi) \exp(-\lambda_m z^*), \quad (21)$$

where the temperature θ_1 is the solution to the following ordinary differential equation:

$$u_z^* D = \frac{d^2\theta_1}{d\xi^2} + Gf(\xi) \quad (22a)$$

subject to the boundary conditions:

$$\left. \frac{d\theta_1(\xi)}{d\xi} \right|_{\xi=0} = 0, \quad (22b)$$

$$\left. \frac{d\theta_1(\xi)}{d\xi} \right|_{\xi=1} = 0. \quad (22c)$$

The solution to Eq. (22) is

$$\theta_1(\xi) = \int_0^\xi (\xi - \xi') (u_z^* D - Gf(\xi')) d\xi' \quad (23a)$$

where

$$D = \frac{\int_0^1 Gf(\xi') d\xi'}{\int_0^1 u_z^* d\xi'}. \quad (23b)$$

The eigenfunction ψ_m and the eigenvalue λ_m are determined by solving the eigenvalue problem (Eq. (17a)) subject to the corresponding boundary conditions, i.e.

$$\left. \frac{d\psi_m(\lambda_m, \xi)}{d\xi} \right|_{\xi=0} = 0, \quad (24a)$$

$$\left. \frac{d\psi_m(\lambda_m, \xi)}{d\xi} \right|_{\xi=1} = 0. \quad (24b)$$

The expansion coefficients a_m are obtained from Eq. (20).

The evaluation of the temperature field from Eqs. (14) and (21) requires the knowledge of the eigenvalues as well as the eigenfunctions of the eigenvalue problem described by Eqs. (17) and (24). These equations are solved numerically using the Runge–Kutta methods, and as many eigenvalues as required are determined accurately without missing any eigenvalues.

2.5. Low-volume flow rate and bulk temperature calculation

In extrusion processing, the flow in the downchannel direction is primarily a combination of drag and pressure flows. For pure drag flow, the downchannel velocity, u_z^* , of the fluid increases monotonically from its screw root value to the maximum value at the moving barrel. However, as the value of the positive pressure gradient increases from zero, a back flow in the z^* direction appears adjacent to the screw root in the u_z^* profile. The strength of the back flow and the size of the back flow region depend on conditions such as the positive pressure gradient, the shear viscosity material function of the fluid, and the volume flow rate. For example, as the volume flow rate is decreased, the pressurization rate increases and hence the back flow, i.e., negative velocity zone becomes more pronounced.

For the condition of positive z -velocity everywhere in the channel, i.e., $u_z^* \geq 0$, the energy equation is only marginally elliptic and can therefore be taken as suitably parabolic. However, when back flow occurs (i.e., $u_z^* < 0$) in some region of the channel, as is the case for high

positive pressure gradient and low-volume flow rate, the energy equation is no longer strictly parabolic. This is manifested in increasing difficulty in obtaining the high-order eigenvalues and eigenfunctions of the eigenvalue problem. But since the contribution of an eigenvalue to the temperature solution is attenuated as the order of the eigenvalue increases, especially far downstream, the accuracy of the solution is not affected by the high-order terms. Other solution techniques based on finite differencing scheme or finite element method have experienced similar difficulties for this energy problem with significant back flow (Lawal and Kalyon, 1994b; Lawal et al., 1996). For example, the Streamline Upwind/Petrov Galerkin (SUPG) technique was applied in a finite element method (Lawal and Kalyon, 1994b; Lawal et al., 1996) to suppress the numerical instability created by the convection terms. The procedure was successful for a range of flow rate values, but for volume flow rate below a critical value, the suppression capability of SUPG breaks down and the solution becomes unstable.

Related to the existence of a back flow region is the conceptual difficulty of evaluating a temperature representative of the fluid at any downchannel location. By convention, a bulk or mixing-up temperature which is an easily measurable quantity is determined. For our flow configuration, the bulk temperature will be defined by

$$\theta_b = \frac{\int_0^1 \theta(\zeta, z^*) u_z^* d\zeta}{\int_0^1 u_z^* d\zeta} \quad (25)$$

However, on closer examination, Eq. (25) is only applicable when the velocity profile is of the same sign throughout, e.g., $u_z^* \geq 0$, and will provide a grossly inaccurate result when a back flow region appears somewhere in the flow region and the size is significant, as may be the case for the low volume flow rate operating condition. The denominator of Eq. (25) arises from the volume flow rate which is operationally always positive. The negative contribution of the back flow region to the numerator of Eq. (25) can result in a bulk temperature that is much less than the entrance temperature, a situation that is physically unrealistic for this viscous heating dominated flow. Here we suggest a modification to the application of Eq. (25) which provides realistic bulk temperature results regardless of the flow profile.

The flow region is delineated according to the sign of the velocity u_z^* , and Eq. (25) is applied locally to each region. For example, if there are two sign changes in the flow profile, there will be three such regions, with the velocity u_z^* in each region having the same sign. The bulk temperature of each local region so obtained is weighted by the ratio of the absolute value of its volume flow rate to the sum of the absolute value of the volume flow rate from each region. The overall bulk temperature is then

obtained by summing up these weighted bulk temperatures, i.e.

$$\theta_b = \frac{\sum_{l=1}^{\text{no. of regions}} (\int_l \theta(\zeta, z^*) u_z^* d\zeta / \int_l u_z^* d\zeta) |\int_l u_z^* d\zeta|}{\sum_{l=1}^{\text{no. of regions}} |\int_l u_z^* d\zeta|} \quad (26)$$

Eq. (26) is consistent as it reverts to Eq. (25) for $u_z^* \geq 0$ throughout the flow region.

3. Results and discussion

The non-linear equations for the values of the extremum locations λ_1 , λ_2 , and λ^* of the velocity profiles were solved using the Newton–Raphson technique with a general relative tolerance of 10^{-6} . The eigenvalues and eigenfunctions of Eqs. (17) and (24) were obtained with the same general relative tolerance except for eigenvalues of order 40 and higher which had a relative tolerance of 10^{-4} . However, it was generally observed that close to the entrance of the extruder, beyond 40 terms there were no significant differences in the series solution (Eqs. (14) and (21)) for the temperature distributions for the range of parameters considered in this study. In addition, as we proceed downstream, the number of terms required to achieve the same accuracy reduces considerably, to the extent that far downstream, not more than 10 terms need be retained.

Detailed comparisons of the analytical solutions for the isothermal velocity profiles with results available in the literature had been reported in our earlier studies (Lawal et al., 1993; Lawal and Kalyon, 1997), and will therefore not be repeated here. Also, in the latter study, the analytical solutions for the temperature distributions were compared with experimental transverse temperature measurements of Esseghir and Sernas (1991) in a single-screw extruder. The agreement was good, and the differences were accounted for in part by the neglect of the curvature effect in the analysis. The experimental temperature measurements of Esseghir and Sernas (1991) were collected on fluids that neither exhibited viscoplasticity nor slip at the wall behavior, hence these measurements were not adequate for complete verification of the applicability of the analytical solutions developed in this study. In addition, the back flow was negligible at the processing and operating conditions used in their experimental study. Experimental pressure gradient and temperature measurements that meet these requirements are therefore needed, but are rather rare in the literature. In fact, the only reliable experimental data on low mass flow rate extrusion of a fluid which exhibits both viscoplasticity and wall slip are reported in the thesis of Yaras (1995), and comparisons will be made between these data and our solutions. However, before these comparisons are

Table 2

The geometry, operating conditions, and material parameters used in the experiment

Material parameters

Herschel–Bulkley fluid

Shear-rate sensitivity parameter $n = 0.43$

$m = 6888 \text{ Pa s}^{0.43}$

$\tau_o = 20 \text{ Pa}$

Navier's wall slip coefficient $= 9.6 \times 10^{-8} \text{ m/Pa s}$

Density $= 1050.6 \text{ kg/m}^3$

Specific heat capacity $= 1078 \text{ J/kgK}$

Thermal conductivity $= 0.206 \text{ W/mK}$

Channel dimensions

Channel depth $= 1.15 \times 10^{-2} \text{ m}$

Channel width $= 2.54 \times 10^{-2} \text{ m}$

carried out, we first examine typical velocity and temperature profiles. The parameters used are as shown in Table 2 unless otherwise indicated in the figures. For constant density, volume flow rate and mass flow rate can, and will henceforth be used interchangeably.

For the conditions of Table 2, the effect of wall slip on the pressurization capability of the extruder when both the screw and barrel surfaces have the same slip coefficient β , is shown in Fig. 3a. As the wall slip coefficient β increases, the mass flow rate decreases for the same pressurization capability. For every β value, above a certain pressure gradient, it is not possible to achieve a positive mass flow rate. Wall slip reduces the velocity gradients, thereby reducing the pressure gradient. If wall slip is ignored, i.e. the Navier's slip coefficient β is taken as zero, the velocity of the fluid at any solid surface takes on the same value as that of the surface. However, on incorporation of wall slip as seen from Fig. 3b, the fluid velocity at either the screw surface or the barrel wall attains a non-zero value. At the screw root, as the slip coefficient increases, so does the fluid velocity. Since the same mass flow rate is imposed, in order to satisfy the mass conservation constraint, we would expect that the increase in fluid velocity in the screw root region will be compensated for by a reduction in the fluid velocity as the barrel surface is approached. This is clearly observable in Fig. 3b where at the barrel surface, the fluid's velocity decreases as the slip coefficient β increases. The velocity gradient at the two solid surfaces exhibits the same behavior, i.e. increasing with β at the screw root but decreasing at the barrel surface.

Fig. 3c presents corresponding dimensionless transverse temperature profiles for different values of β at a selected axial location, $z^* = 10^{-2}$ for the isothermal barrel and adiabatic screw, with the entrance temperature different from the barrel temperature. For each β value, the velocity gradient increases from the screw surface to the barrel surface and thus the viscous dissipation effect. The dimensionless temperature rise, therefore,

increases from the screw surface (Fig. 3c) to some point in the region near the barrel surface where it attains a maximum value and is subsequently forced to reduce in order to meet the barrel wall temperature constraint. The fluid is essentially heating the barrel due to significant viscous dissipation effects. At any transverse location ξ , the dimensionless temperature rise decreases as the slip coefficient β increases. In the region close to the barrel, viscous dissipation dominates, and since increase in β results in decreased velocity gradient in this region (Fig. 3b), the dimensionless temperature rise decreases as β increases. In the screw root region, axial convection seems to be the dominant heat transfer mechanism as opposed to viscous dissipation. Even though the velocity gradient here decreases as β increases, the increased axial convection effect gives rise to a reduction in the dimensionless temperature rise.

The effect of the yield stress on the mass flow rate achievable given the desired pressurization rate or vice versa is shown in Fig. 4a. At low values of the pressurization rate, the yield stress exerts no significant influence on the mass flow rate. At higher pressurization rate, i.e. greater than 20 MPa/m, as the yield stress increases, the mass flow rate increases at constant pressurization (or conversely, pressurization rate increases at constant mass flow rate). This is related to the increased shear viscosity of the fluid as the yield stress increases. The corresponding velocity profiles are shown in Fig. 4b. In the screw root region, the fluid's velocity increases as the yield stress increases while the velocity gradient decreases. The reverse behavior is obtained at the barrel surface. In the light of the velocity profiles, we can now examine the effect of the yield stress on the temperature profiles. For the adiabatic screw condition, at high values of τ_o , the dimensionless temperature rise increases from its value at the screw surface and subsequently decreases to the prescribed barrel temperature with the maximum fluid temperature occurring at a transverse location dependent on the value of τ_o . In addition, the temperature everywhere exceeds that of the barrel. In contrast, at lower values of τ_o , the dimensionless temperature rise monotonically decreases from the screw root value to that of the barrel. At any transverse location, increased τ_o gives rise to increased dimensionless temperature rise.

The effect of mass flow rate on the downchannel velocity u_z^* distributions is shown in Fig. 5. At high mass flow rate, the flow in the downchannel direction is dominated by drag, and the generated pressure gradient is low. The velocity values are positive throughout. At low mass flow rate, a back flow region with negative velocity ($u_z^* < 0$) appears adjacent to the screw root, its size and strength increase as the mass flow rate decreases, and the generated pressure gradient correspondingly increases. The transverse temperature distributions corresponding to the velocity profiles at two downchannel

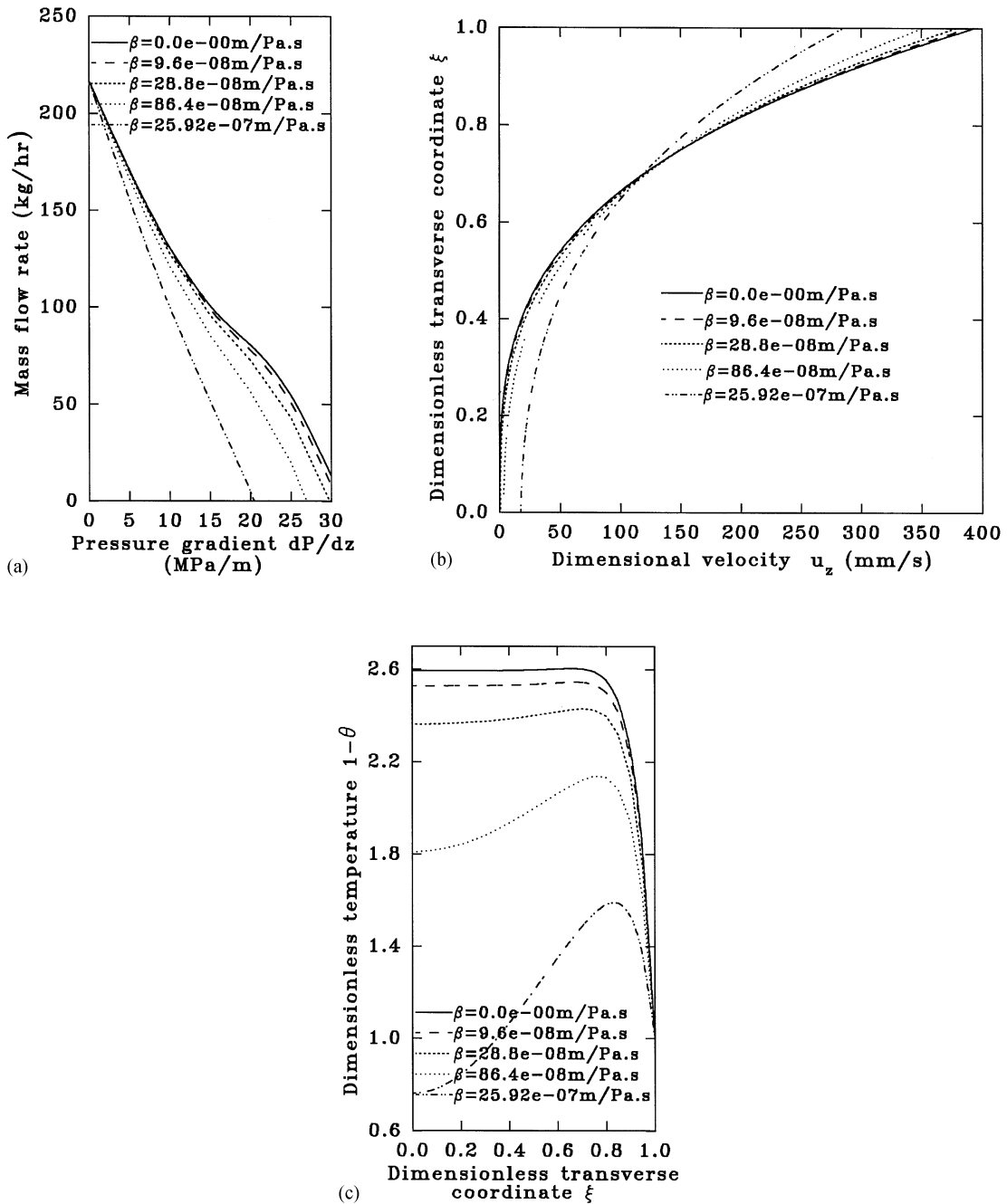


Fig. 3. (a) Mass flow rate vs. pressure gradient relationship for an extruder for varying slip coefficient β with the screw and barrel having the same slip coefficient. (b) Dimensional transverse velocity profiles in an extruder channel for varying slip coefficient β . (c) Dimensional transverse temperature profiles in an extruder channel with adiabatic screw root and isothermal barrel for varying slip coefficient β .

locations are presented in Fig. 6a and b. The thermal boundary condition is that of isothermal barrel and adiabatic screw, with the entrance temperature lower than the barrel temperature. In the entrance region (Fig. 6a), the temperature distribution is dictated primarily by the interplay between the downchannel convection term and the viscous heat generated. In the region close to the barrel surface, generally as the mass flow rate reduces,

the velocity gradient increases and in contrast, the downchannel velocity u_z^* decreases. Increased velocity gradient results in higher viscous energy dissipation and decreased downchannel velocity leads to increased temperature rise. In effect, in the barrel region, the temperature rise experienced by the fluid increases as the mass flow rate decreases. For low-mass flow rate values, the temperature is almost everywhere higher than the barrel

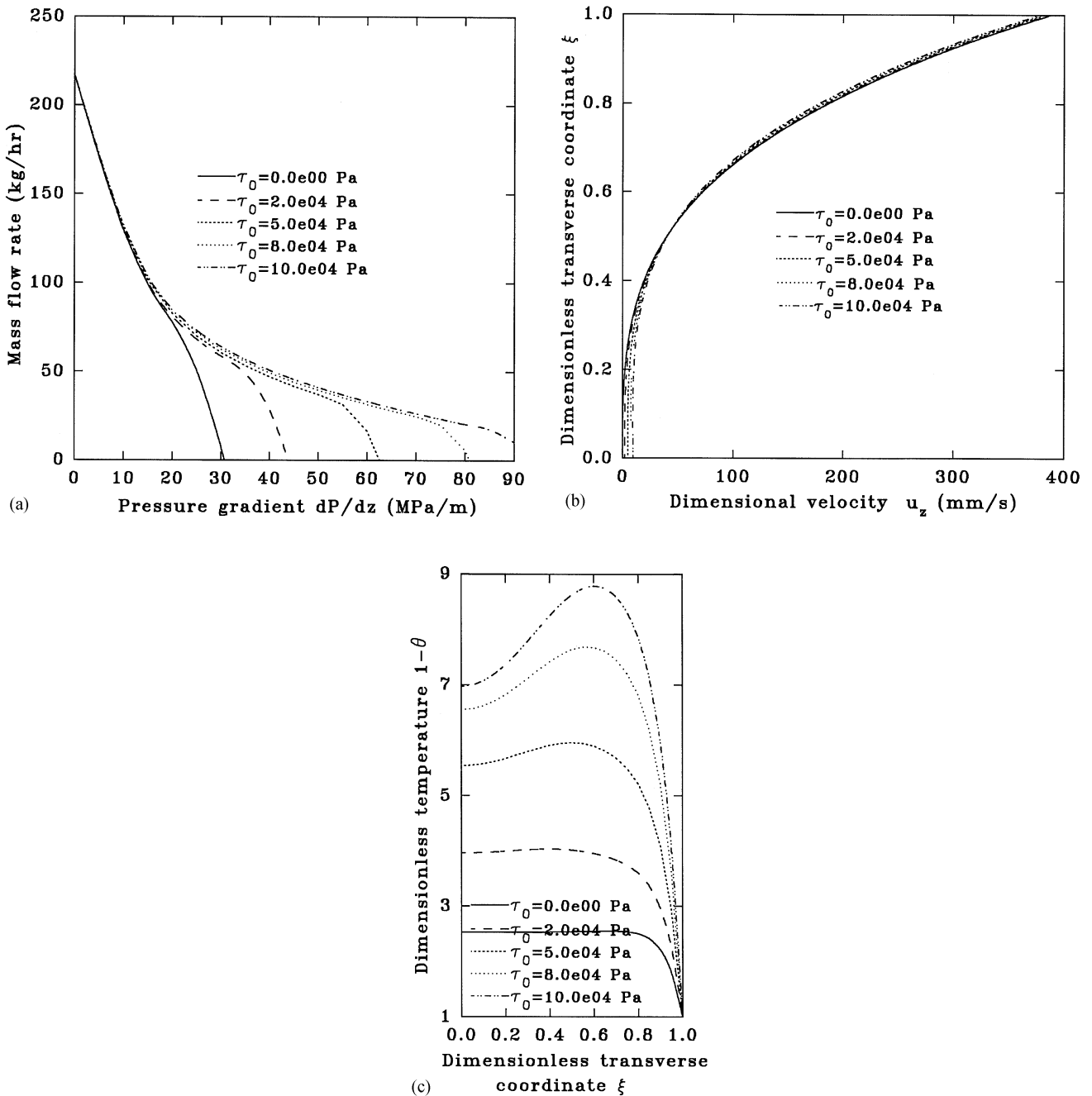


Fig. 4. (a) Mass flow rate vs. pressure gradient relationship for an extruder for varying apparent yield stress τ_0 . (b) Dimensional transverse velocity profiles in an extruder channel for varying apparent yield stress τ_0 . (c) Dimensional transverse temperature profiles in an extruder channel with adiabatic screw and isothermal barrel for varying apparent yield stress τ_0 .

temperature whereas for high-mass flow rate, the barrel temperature is greater than the fluid temperature.

As observed in Fig. 6a, a significant portion of the temperature rise of the fluid occurs within a short distance from the barrel surface since the velocity gradients are highest in this region and hence the viscous dissipation effect. Thereafter, the requirement of an adiabatic screw surface which does not allow for the viscous heat

generated to be dissipated through the screw surface will result in a small temperature change, and an almost flat temperature profile as the screw surface is approached. Besides, the velocity gradients are not particularly high in the screw region, and so also the downchannel velocity u_z^* values. As we proceed downstream of the extruder (e.g. Fig. 6b), the effect of the conduction from the barrel surface becomes more pronounced and the fluid

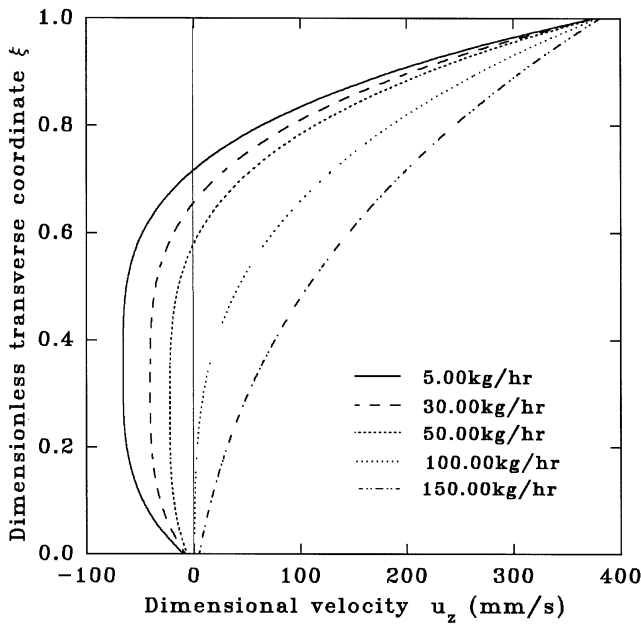


Fig. 5. Dimensional downchannel velocity profiles in an extruder channel for varying mass flow rate (screw speed = 155 rpm, and $\beta_t = \beta_b = 28.8 \times 10^{-8}$ m/Pa s)

temperature is now everywhere higher than the wall temperature, or almost the same as the wall temperature, even for high-mass flow rates.

Another thermal boundary condition that is of practical interest is that of isothermal barrel and screw surfaces with both at the same temperature. This thermal boundary condition can be attained in practice if there is an effective circulatory flow in the extruder (Fenner, 1969). Since the fluid's properties are assumed to be temperature independent, the velocity profiles are unaffected by the change in thermal boundary conditions, and are hence as presented in Fig. 5. The corresponding temperature distributions at two downchannel locations are shown in Fig. 7a and b. The effect of the mass flow rate on the temperature rise is qualitatively similar to that for the adiabatic screw thermal boundary condition. However, unlike the adiabatic screw results, with the temperature of both barrel and screw surfaces fixed, the maximum temperature rise is forced to occur within the fluid rather than at either of the two solid boundaries.

The analytical solutions will now be compared with the experimental pressure gradient and bulk temperature measurements obtained from the work of Yaras (1995) on twin-screw extrusion of a highly concentrated suspension which exhibits viscoplasticity and apparent wall slip. The fluid's properties, as well as the processing and operating conditions of the extruder are as indicated in Table 2. At the relatively low mass flow rates used in the experiments, the axial pressure gradients were constant, implying that variations in the shear viscosity due to temperature were insignificant. The shear viscosity values

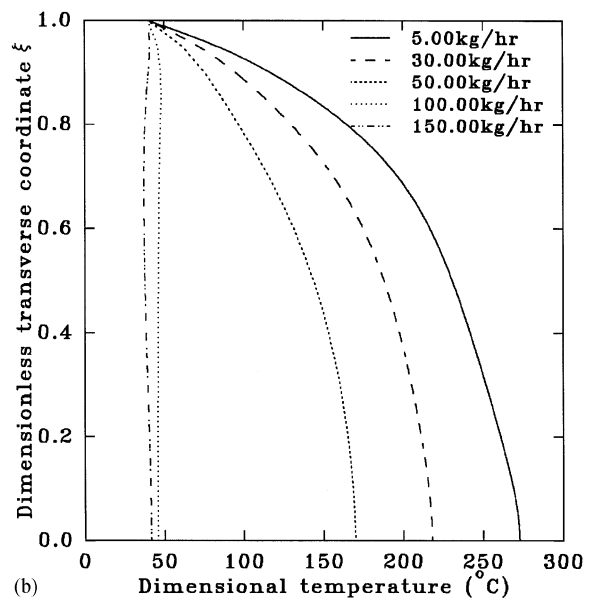
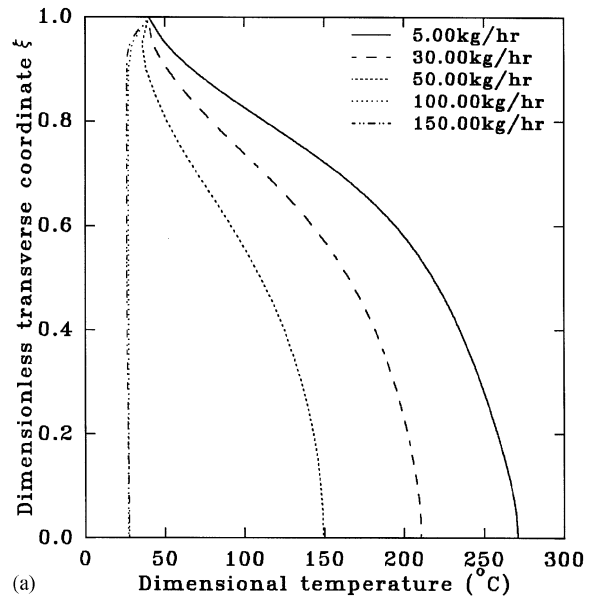


Fig. 6. Dimensional temperature profiles in an extruder channel with adiabatic screw root and isothermal barrel for varying mass flow rate at (a) $z^* = 6 \times 10^{-4}$ and (b) $z^* = 6 \times 10^{-3}$ ($T_o = 298$ K, $T_w = 313$ K).

can therefore be evaluated at a selected temperature which in this case is the bulk temperature at the entrance. The downchannel pressure gradient corresponding to one third of the experimental flow rate (since there are three channels in the extruder) was then obtained from the analytical solutions for each set of experimental conditions. These values were converted to the corresponding axial pressure gradient using the helix angle ϕ (Booy, 1978):

$$\frac{dP_m}{dz} = \frac{dP_m}{dl} \sin \phi \sqrt{\frac{1 + \tan^2 \phi}{\rho_c^2/4 + \tan^2 \phi}}, \quad (27)$$

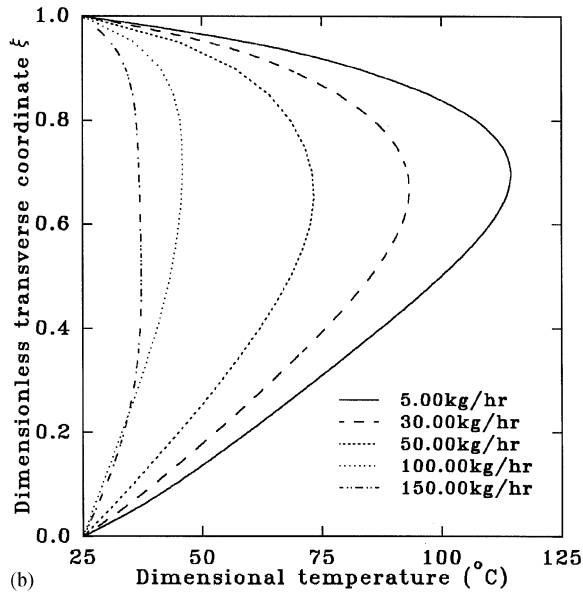
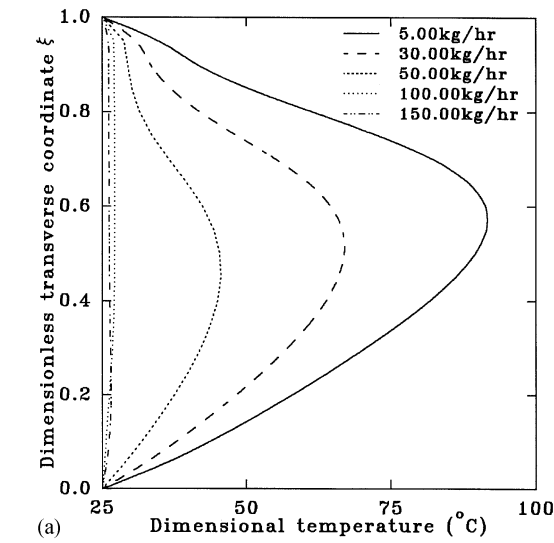


Fig. 7. Dimensional temperature profiles in an extruder channel with isothermal screw and barrel for varying mass flow rate at (a) $z^* = 6 \times 10^{-4}$ and (b) $z^* = 6 \times 10^{-3}$ ($T_w = 298$ K).

where ρ_c is the ratio of the centerline distance to screw radius. To convert to actual pressure values, ambient pressure is assumed at the beginning of the filled length. In Figs. 8–11, the typical experimental pressure distributions are compared with the predictions of the analytical solutions for a wide range of screw rpm. The excellent agreement suggests that when the wall slip behavior of the fluid and its shear viscosity are adequately characterized, the analytical predictions for the pressure distributions of this study will be reliably accurate, provided that the shear viscosity of the fluid is not strongly dependent on the temperature.

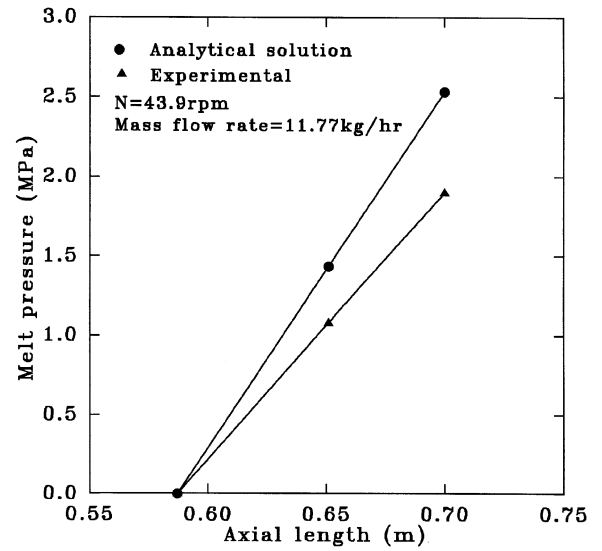


Fig. 8. Comparison of experimental and predicted pressure at 43.9 rpm and 11.77 kg/h.

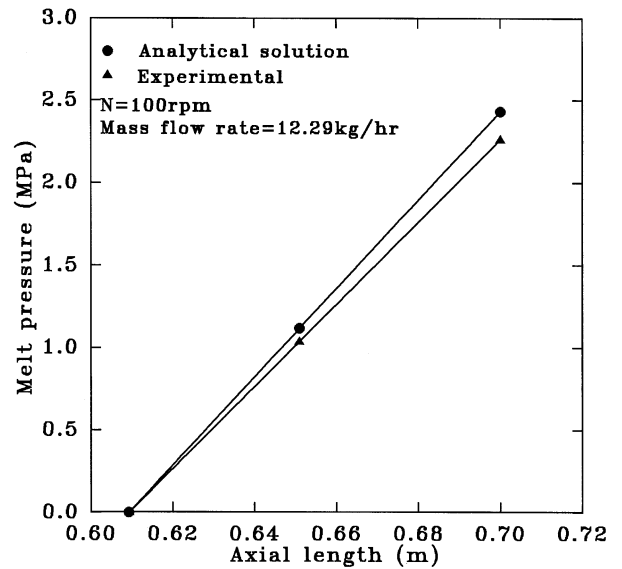


Fig. 9. Comparison of experimental and predicted pressure at 100 rpm and 12.29 kg/h.

In Fig. 12, the experimentally obtained bulk temperature values are compared with the analytical results for four different screw rpm values. In the low screw rpm range (i.e. $\omega < 80$), the agreement is good, and the differences are indeed within the experimental accuracy range. However, as the screw rpm increases, the experimental temperature measurements and the analytical results diverge for this low-mass flow rate condition. An examination of the bulk temperature variation with mass flow rate (Figs. 13–15) at selected downchannel locations for three different screw rpm values may provide an

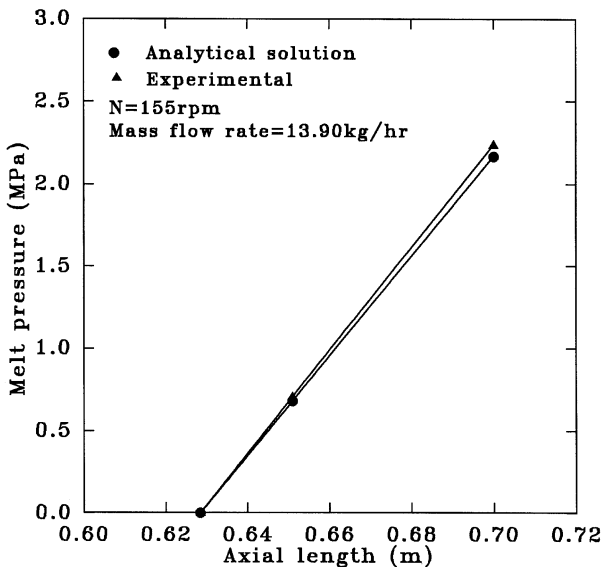


Fig. 10. Comparison of experimental and predicted pressure at 155 rpm and 13.90 kg/h.

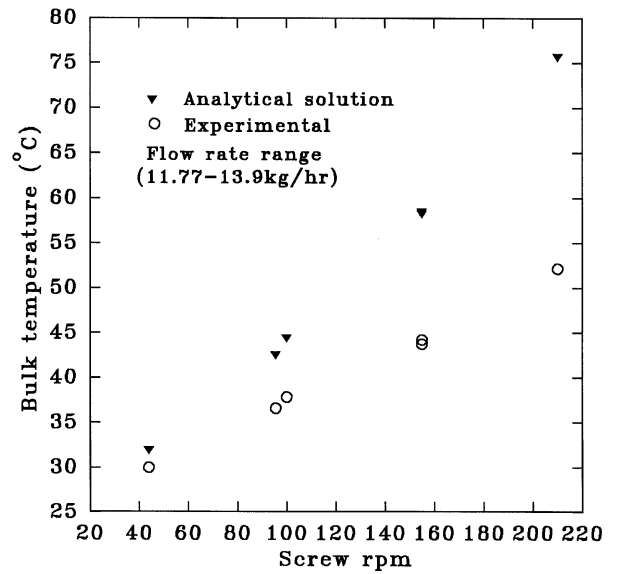


Fig. 12. Comparison of experimental and predicted bulk temperatures at various screw rotational speeds.

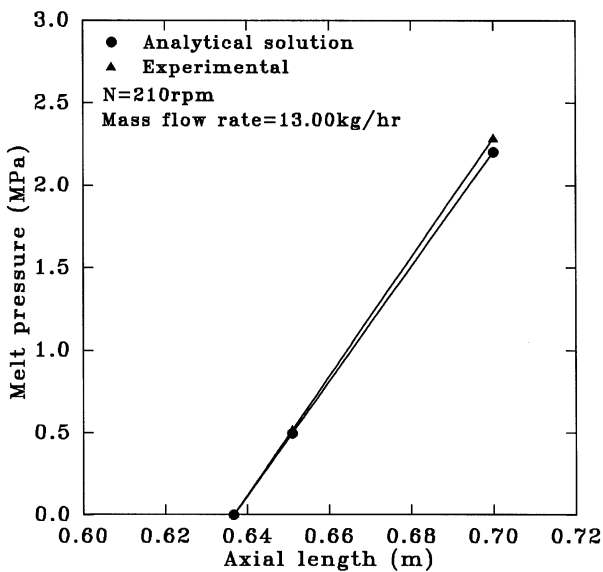


Fig. 11. Comparison of experimental and predicted pressure at 210 rpm and 13.00 kg/h.

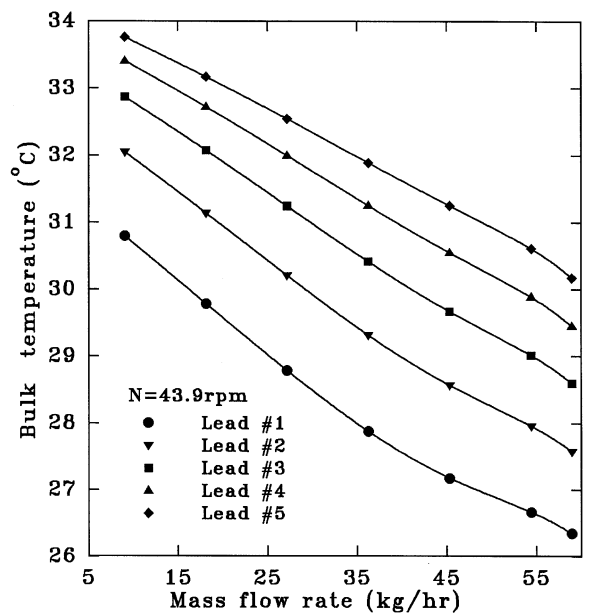


Fig. 13. Bulk temperature vs. mass flow rate at different screw leads for screw speed of 43.9 rpm.

explanation for the disagreement at high screw rpm range. As indicated in Figs. 13–15, the bulk temperature increases as the mass flow rate decreases as a result of increased viscous dissipation with decreased flow rate (Figs. 6 and 7), regardless of the screw rpm value. This behavior is not expected for the low-mass flow rate–high screw rpm regime where in the pseudo three-dimensional numerical simulation (Lawal et al., 1996), it was observed that the presence of the transverse convection terms results in increased viscous energy generated with

increased mass flow rate. In the low screw rpm–low-mass flow rate regime, the results of the present study and those reported in Lawal et al. (1996) are in excellent agreement, since the importance of the transverse convection terms diminishes as the screw rpm decreases. A similar outcome was obtained for the high mass flow rate regime, where regardless of the screw rpm, the down-channel convection term is more dominant than the transverse convection terms. In essence, the analytical

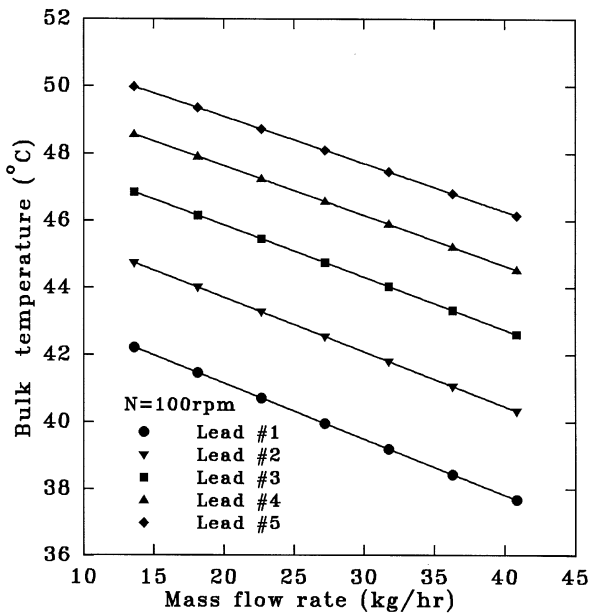


Fig. 14. Bulk temperature vs. mass flow rate at different screw leads for screw speed of 100 rpm.

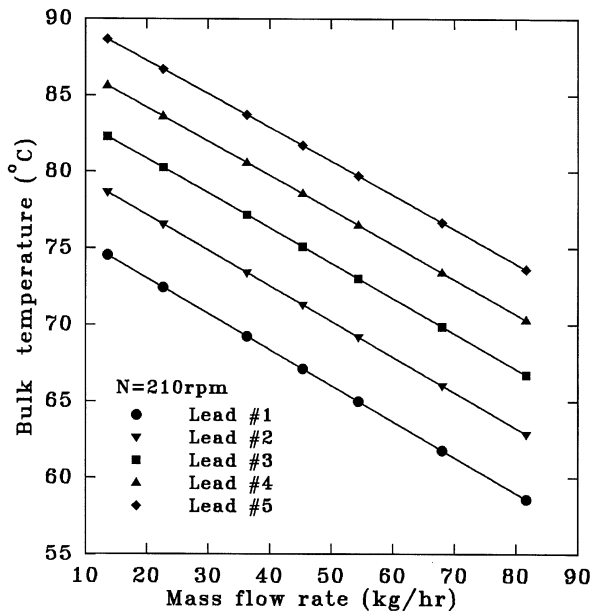


Fig. 15. Bulk temperature vs. mass flow rate at different screw leads for screw speed of 210 rpm.

temperature solutions will correctly predict the temperature distributions in the extruder except in the low-mass flow rate–high screw rpm regime. The mass flow rate limit for the applicability of the analytical temperature distributions depends on the screw rpm. As the screw rpm increases, so does the value of this limit. For the experimental conditions used in the study of Yaras (1995), the limiting values for the mass flow rate are

approximately 27 and 45 kg/h for screw rpm values of 100 and 210 respectively.

4. Conclusions

In this paper, we have developed general analytical and exact solutions for the nonisothermal analysis of extrusion processing of viscoplastic fluids with significant back flow. The model accommodates the interfacial flow boundary condition of slip at the wall generally encountered with concentrated suspensions and filled polymers. The developed solutions can be used in assessing the importance of such parameters as the slip coefficient (β_t and β_b), the apparent yield stress τ_o , the Griffith number, and the Peclet number on single and twin-screw extrusion processing.

The analytical solutions have been compared with experimental pressure gradient and bulk temperature measurements obtained from twin-screw extrusion processing of concentrated suspensions at low mass flow rate where there exists significant back flow. For these suspensions with a low-temperature coefficient of viscosity, the predicted pressure gradient is in excellent agreement with the experimental data, and the results of this study as well as those of earlier studies (Lawal and Kalyon, 1994b; Lawal et al., 1996) show that wall slip behavior (if present) must be properly accounted for, and the rheological behavior of the fluid carefully characterized if the analytical solutions are to be used for design purposes. Comparisons of bulk temperature measurements indicate that the analysis can be reliably used in predicting temperature distributions provided that the screw rpm is not very high when the mass flow rate is low.

Acknowledgements

One of us, A.L. would like to express his gratitude to KFUPM for making available some of the computing facilities required for the completion of the work. The typing of the manuscript was excellently done by Mr. E. Esteban.

Notations

a_m	expansion coefficient defined by Eq. (14) or Eq. (21)
b_1 – b_4	coefficients used in Eq. (16) and given in Table 1
Bi_0	Biot modulus at screw surface
Bi_1	Biot modulus at barrel surface
$c(y)$	inlet temperature distribution
$C(\xi)$	dimensionless inlet temperature distribution
C_p	specific heat capacity

dP/dz	pressure gradient
$f(\xi)$	viscous dissipation function defined by Eq. (13)
G	Griffith number
h_0	heat transfer coefficient at screw surface
h_1	heat transfer coefficient at barrel surface
H	channel depth
k	thermal conductivity
l	axial coordinate direction
m	material parameter
n	parameter governing the sensitivity of fluid to deformation rate
\mathbf{n}	unit outward normal vector
$P\acute{e}$	Péclet number
s	reciprocal of n
\mathbf{t}	unit tangent vector
T	temperature
T_o	entrance temperature
T_w	barrel temperature
T^*	reference temperature
\mathbf{u}	velocity vector of fluid
$\mathbf{u}_{\text{solid}}$	velocity vector of solid surface
u_z	velocity in the z -coordinate direction
u_z^*	dimensionless velocity in the z -coordinate direction
V_w	linear screw velocity
y	y -coordinate transverse direction
z	z -coordinate downchannel direction
z^*	dimensionless z -coordinate

Greek letters

α_1	dimensionless slip coefficient at the screw surface
α_2	dimensionless slip coefficient at the barrel surface
β	Navier's slip coefficient
β_b	slip coefficient at the screw surface
β_t	slip coefficient at the barrel surface
$ \dot{\gamma} $	magnitude of the deformation rate
Λ	dimensionless pressure gradient defined by Eq. (3a)
ψ_m	eigenfunction of eigenproblem defined by Eqs. (17a)–(17c)
η	shear viscosity material function
κ_1	dimensionless ratio of slip coefficient to yield stress at the screw surface

κ_2	dimensionless ratio of slip coefficient to yield stress at the barrel surface
λ_m	eigenvalues of eigenproblem defined by Eqs. (17a)–(17c)
$\boldsymbol{\pi}$	total stress tensor
ϕ	helix angle
θ	dimensionless temperature defined by Eq. (11a)
θ_b	dimensionless bulk temperature defined by Eq. (25) or Eq. (26)
ρ	fluid density
τ_o	apparent yield stress
τ_{yz}	shearing stress
ξ	dimensionless transverse coordinate defined by Eq. (3a)
ω	screw rpm

References

- Aral, B., & Kalyon, D.M. (1994). *J. Rheol.*, 38, 957.
- Aral, B., & Kalyon, D.M. (1995). *Plast. Rubber Comp. Proc. Appl.*, 24, 201.
- Bird, R.B., Dai, G.C., & Yarusso, B.J. (1983). *Rev. Chem. Engng*, 1, 1.
- Booy, M.L. (1978). *Polym. Engng Sci.*, 20, 1220.
- Colwell, R.E., & Nicholls, K.R. (1959). *Ind. Engng Chem.*, 51, 841.
- Denson, C.D., & Hwang, B.K. (1980). *Polym. Engng Sci.*, 20, 965.
- Esseghir, M., & Sernas, V. (1991). SPE Antec Technical Paper 37, 54.
- Fenner, T.R. (1969). Ph.D. thesis, University of London
- Griffith, R.M. (1962). *Ind. Engng Chem. Fund.*, 1, 180.
- Kalyon, D.M., Gotsis, A.D., Yilmazer, U., Gogos, C., Sangani, H., Aral, B., & Tsenoglou, C. (1988). *Adv. in Polymer Technol.*, 8, 337.
- Kalyon, D.M., Yaras, P., Aral, B., & Yilmazer, U. (1993). *J. Rheol.*, 37, 35.
- Kwon, T.H., Jaluria, Y., Karwe, M.V., & Sastrohartono, T. (1991). In A.I. Isayev (Ed.), *Modeling of polymer processing (recent developments)*. Hanser Publishers.
- Lai-Fook, R.A., Senouci, A., & Smith, A.C. (1989). *Polym. Engng Sci.*, 29, 433.
- Lawal, A., & Kalyon, D.M. (1994a). *Polym. Engng Sci.*, 34, 1471.
- Lawal, A., & Kalyon, D.M. (1994b). *Num. Heat Transfer*, 26, 103.
- Lawal, A., & Kalyon, D.M. (1997). *Int. J. Heat Mass Transfer*, 40, 3883.
- Lawal, A., Railkar, S., Yaras, P., & Kalyon, D.M. (1996). *J. Mater. Process. Manuf. Sci.*, 5, 57.
- Lawal, A., Yilmazer, U., & Kalyon, D.M. (1993). *Chem. Engng Comm.*, 122, 127.
- Silliman, W.T., & Scriven, L.E. (1980). *J. Comp. Phys.*, 34, 287.
- Wang, Y., & White, J.L. (1989). *J. Non-Newtonian Fluid Mech.*, 32, 19.
- Yaras, P. (1995). Ph.D. thesis, Stevens Institute of Technology, Hoboken, NJ.
- Yilmazer, U., & Kalyon, D.M. (1989). *J. Rheol.*, 33, 1197.
- Zamodits, H.J., & Pearson, J.R.A. (1969). *Trans. Soc. Rheol.*, 13, 357.